JCI insight

RESEARCH ARTICLE

Severe acute respiratory disease in American mink experimentally infected with SARS-CoV-2

Danielle R. Adney,[1,2] Jamie Lovaglio,[3] Jonathan E. Schulz,[1] Claude Kwe Yinda,[1] Victoria A. Avanzato,[1] Elaine Haddock,[1] Julia R. Port,[1] Myndi G. Holbrook,[1] Patrick W. Hanley,[2] Greg Saturday,[3] Dana Scott,[3] Carl Shaia,[3] Andrew M. Nelson,[2] Jessica R. Spengler,[4] Cassandra Tansey,[4] Caitlin M. Cossaboom,[4] Natalie M. Wendling,[4] Craig Martens,[5] John Easley,[6] Seng Wai Yap,[7] Stephanie N. Seifert,[8] and Vincent J. Munster[1]

[1]Laboratory of Virology, Division of Intramural Research, National Institute of Allergy and Infectious Diseases, National Institutes of Health, Hamilton, Montana, USA. [2]Lovelace Biomedical Research Institute, Department of Comparative Medicine, Albuquerque, New Mexico, USA. [3]Rocky Mountain Veterinary Branch, Division of Intramural Research, National Institute of Allergy and Infectious Diseases, National Institutes of Health, Hamilton, Montana, USA. [4]Centers for Disease Control and Prevention, Atlanta, Georgia, USA. [5]Research Technologies Branch, National Institute of Allergy and Infectious Diseases, National Institutes of Health, Hamilton, Montana, USA. [6]Mink Veterinary Consulting and Research Service, Glenbeulah, Wisconsin, USA. [7]Department of Surgical Sciences, School of Veterinary Medicine, University of Wisconsin-Madison, Madison, Wisconsin, USA. [8]Paul G. Allen School for Global Health, Washington State University, Pullman, Washington, USA.

An animal model that fully recapitulates severe COVID-19 presentation in humans has been a top priority since the discovery of SARS-CoV-2 in 2019. Although multiple animal models are available for mild to moderate clinical disease, models that develop severe disease are still needed. Mink experimentally infected with SARS-CoV-2 developed severe acute respiratory disease, as evident by clinical respiratory disease, radiological, and histological changes. Virus was detected in nasal, oral, rectal, and fur swabs. Deep sequencing of SARS-CoV-2 from oral swabs and lung tissue samples showed repeated enrichment for a mutation in the gene encoding nonstructural protein 6 in open reading frame 1ab. Together, these data indicate that American mink develop clinical features characteristic of severe COVID-19 and, as such, are uniquely suited to test viral countermeasures.

Introduction

Development of animal models has been a critical need since the emergence of SARS-CoV-2 to test vaccines and viral countermeasures (1). Multiple SARS-CoV-2 models of traditional laboratory species, including mice, hamsters, ferrets, and nonhuman primates, have been developed (2–6). However, many of these models either result in mild to moderate disease, experience distinctive viral dissemination due to altered angiotensin-converting enzyme 2 (ACE2) expression, specifically in the brain, or fail to develop clinical acute respiratory disease syndrome (ARDS) (2, 3, 6). SARS-CoV-2 in experimentally infected mink is known to cause pathogenesis reminiscent of severe COVID-19 in humans (7); however, additional characterization of this model is still needed. This model could allow experimental research into the pathogenesis of severe COVID-19 and would facilitate the evaluation of therapeutic countermeasures in the context of severe disease.

Experimental infections of ferrets resulted in viral replication and transmission to naive individuals but very minimal to mild clinical signs of disease (4, 5). However, this does not appear to be the case for all members of the Mustelidae family (4, 5, 8–10). Reports of farmed mink (*Neogale vison*) infected with SARS-CoV-2 emerged in the Netherlands in April 2020 (11). To date, at least 12 countries have reported outbreaks in farmed mink, and there have been 2 reports describing positive feral or escaped mink (12, 13). While many naturally infected mink exhibited mild to moderate clinical disease, a subset of these animals experienced an acute interstitial pneumonia that manifested with severe respiratory distress (11, 14). Genomic surveillance in samples originating from mink in Denmark identified a series of changes in SARS-CoV-2 spike protein, known as the Cluster 5 variant (15). This mink-associated variant resulted in reduced neutralization with

Conflict of interest: DRA serves as a paid consultant providing expert opinions on disease transmission modeling.

Submitted: February 22, 2022
Accepted: October 11, 2022
Published: November 22, 2022

Reference information: *JCI Insight*. 2022;7(22):e159573. https://doi.org/10.1172/jci.insight.159573.

human convalescent sera in vitro (15). A high susceptibility to infection coupled with the public health risk of intrahost viral evolution prompted massive culls of an estimated 17 million mink on Danish farms (16).

Here, we show that experimentally infected mink develop a severe acute respiratory infection. After infection, progressive respiratory disease can be observed clinically, radiographically, and by histopathology. High amounts of viral RNA and infectious virus can be detected from the respiratory tract. Deep sequencing of SARS-CoV-2 genomes from oral swabs and lung tissue samples collected 3 days post inoculation (dpi) demonstrate rapid enrichment for a nonsynonymous mutation in the gene encoding for the nonstructural protein 6 (nsp6) in ORF1a in lung tissue samples. These data indicate the potential for rapid viral evolution in mink at the human-animal interface in a short time frame. Together, these data suggest that the mink animal model recapitulates severe disease observed in hospitalized and fatal human cases of COVID-19 and could be useful to test countermeasures against severe COVID-19.

Results

Mink ACE2 supports efficient entry of SARS-CoV-2. To evaluate the utility of the mink model for COVID-19, we compared human and mink ACE2 functional receptor entry using structural analysis and a vesicular stomatitis virus pseudotype entry assay (17). The sequence of mink ACE2 was obtained by sequencing from lung tissue. The obtained mink ACE2 sequence is 99.8% identical to the previously published *Neogale vison* ACE2 sequence (GenBank QPL1221.1). Two substitutions are observed at residues 231 and 613, in which the threonine and tyrosine in the previous sequence are replaced by a lysine and a cysteine, respectively. These residues are not located in the SARS-CoV-2 receptor binding domain–ACE2 (SARS-CoV-2 RBD–ACE2) interface. Both American mink *ACE2* sequences are 99% identical to the published European mink *ACE2* sequence (*Mustela lutreola biedermanni*, GenBank QNC68911.1) and approximately 83% identical to human *ACE2* (*Homo sapiens*, GenBank BAB40370.1) (Figure 1A).

To compare differences within the ACE2 interface with the SARS-CoV-2 spike RBD, the residues participating in the interaction, as described by Lan et al. (18), were mapped onto an aa sequence alignment of ACE2 from American mink (*Neogale vison*), European mink (*Mustela lutreola biedermanni*, GenBank QNC68911.1), and humans (*Homo sapiens*, GenBank BAB40370.1) (19). The binding residues are 65% identical between mink and human ACE2, with 7 of the 20 total interface residues differing in mink (Figure 1A). These residues are highlighted on the structure of SARS-CoV-2 RBD bound to human ACE2 to visualize these differences (Figure 1B). Consistent with a previous analysis, critical residues for interaction with the spike RBD, K31, Y41, and Y353 are conserved (19).

To investigate if the observed discrepancies between human and mink ACE2 translate to significant differences in spike entry, we directly compared the viral entry of vesicular stomatitis virus (VSV) SARS-CoV-2 spike pseudotype particles on Baby Hamster Kidney (BHK) fibroblasts (BHK-21 cells, CCL-10; ATCC) transfected with either human or mink ACE2. We observed significantly increased entry in mink ACE2-expressing cells compared with those expressing human ACE2 for the prototype WA1 lineage A SARS-CoV-2 spike (Figure 1C; alignment, entry data, $P = 0.0307$, 2-way ANOVA followed by Holm-Šídák multiple comparisons test). However, the B.1.1.7 (Alpha) variant showed no difference ($P = 0.1505$, 2-way ANOVA followed by Holm-Šídák multiple comparisons test). Overall, the Alpha variant showed slightly increased entry in both human and mink ACE2. Considering both variants together, there was no statistical difference in entry of the spikes to human and mink ACE2 ($P = 0.5633$, 2-tailed t test) (Figure 1C), these data are consistent with viral growth curves (Supplemental Figure 1; supplemental material available online with this article; https://doi.org/10.1172/jci.insight.159573DS1).

We next determined the ACE2 and TMPRSS2 expression in the respiratory tract of mink. ACE2 was multifocally detected in the respiratory olfactory epithelium and there were multifocal SARS-CoV-2 immunoreactive respiratory and olfactory epithelial cells (Supplemental Figure 2). TMPRSS2 was detected in the olfactory epithelial region of the turbinates in contrast to ACE2 immunoreactivity, which was also detected in the lower respiratory bronchiolar epithelium and type I and type II pneumocytes (Supplemental Figure 2).

Experimentally infected mink develop severe respiratory disease by 2 dpi. A total of 11 adult farmed mink were inoculated i.n. and intratracheally with 10^5 $TCID_{50}$ of Alpha variant B.1.1.7 (hCoV-319 19/England/204820464/2020, EPI_ISL_683466). Due to the severity of clinical disease and respiratory distress, 2 animals reached endpoint criteria and were euthanized the evening of 2 dpi. Eight animals reached endpoint criteria at 3 dpi, and 1 animal recovered from severe disease and was euthanized on the predetermined experimental endpoint of 28 dpi.

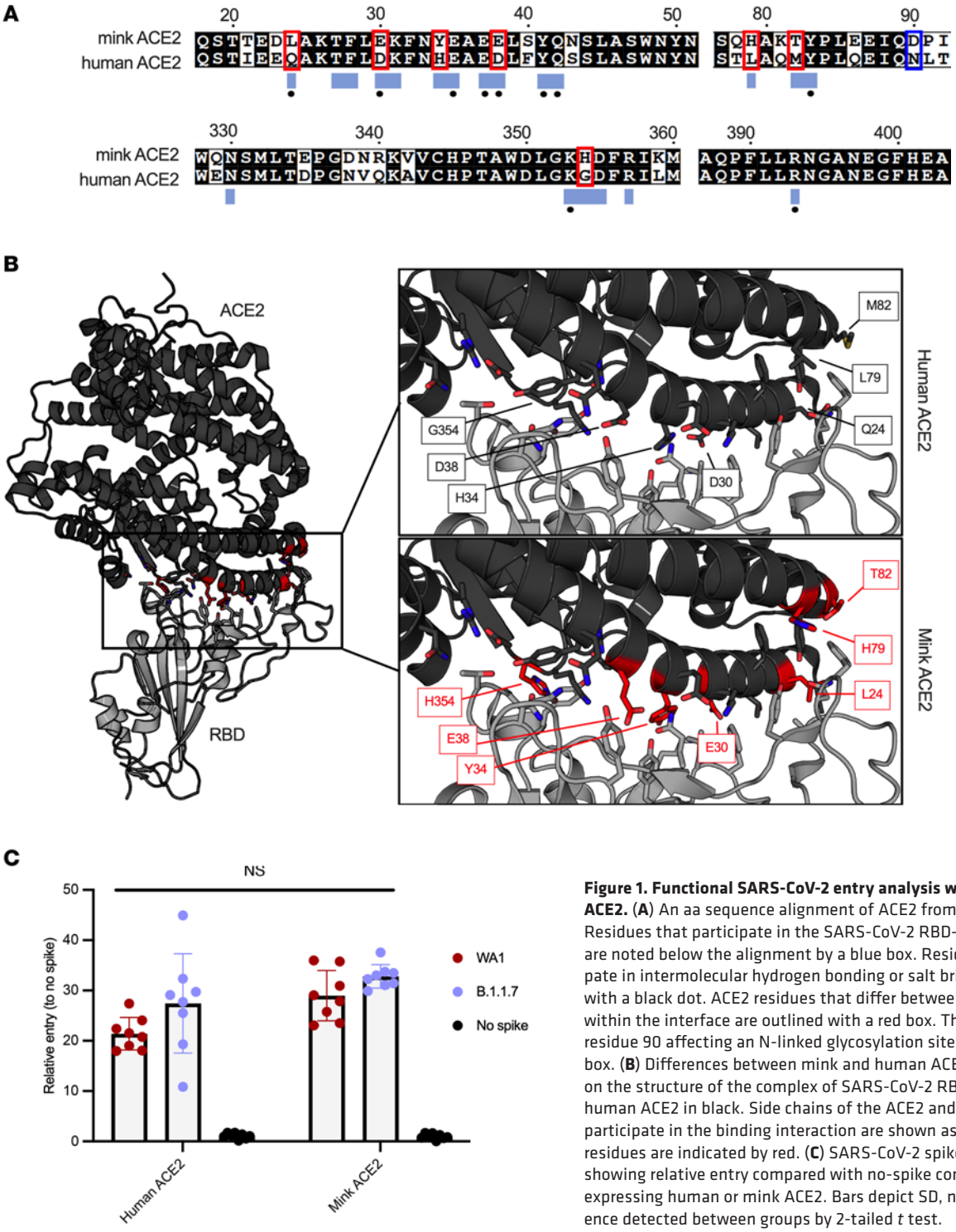

Figure 1. Functional SARS-CoV-2 entry analysis with human and mink ACE2. (**A**) An aa sequence alignment of ACE2 from mink and humans. Residues that participate in the SARS-CoV-2 RBD–ACE2 interaction are noted below the alignment by a blue box. Residues that participate in intermolecular hydrogen bonding or salt bridges are marked with a black dot. ACE2 residues that differ between mink and humans within the interface are outlined with a red box. The substitution at residue 90 affecting an N-linked glycosylation site is noted with a blue box. (**B**) Differences between mink and human ACE2 are highlighted on the structure of the complex of SARS-CoV-2 RBD in gray bound to human ACE2 in black. Side chains of the ACE2 and RBD residues that participate in the binding interaction are shown as sticks. The mutated residues are indicated by red. (**C**) SARS-CoV-2 spike pseudotype assay showing relative entry compared with no-spike control in BHK cells expressing human or mink ACE2. Bars depict SD, no significant difference detected between groups by 2-tailed *t* test.

Marked weight loss (up to 15%) was observed in all animals by 3 dpi (Figure 2A). In the animal that survived infection, BW returned to baseline values by 14 dpi (Supplemental Figure 3A). Clinical signs were first detectable at 1 dpi in 5 of the 11 (45%) animals, with clinical signs observed in 9 of the 11 (82%) animals by 2 dpi and all remaining animals by 3 dpi. Signs of clinical disease included dull mentation, shivering, hunched or balled posture, lethargy, anorexia, increased respiratory effort, tachypnea, and occasional nasal discharge that included both epistaxis and serous discharge (Figure 2, A and B). Animals were examined at 1, 3, 5, 7, 10, 14, 17, 21, and 28 dpi under anesthesia; 10 animals were clinically dehydrated by 3 dpi.

Complete blood count (CBC) and complete chemistry panels were performed on blood samples collected at least 1 week prior to infection and at 0, 1, 3, 5, 7, 10, 14, 17, 21, and 28 dpi. At all time points following infection, the CBC was unremarkable apart from a decreased WBC count characterized by a mild lymphopenia that was most pronounced in the 9 remaining animals at 3 dpi (Figure 2C). The neutrophil/lymphocyte ratio (NLR) was significantly increased at the terminal endpoint for clinically ill animals (Figure 2D). The single surviving animal had an elevated NLR that peaked at 5 dpi as compared with baseline then quickly decreased (Supplemental Figure 3B). The blood chemistry panel was clinically unremarkable for all values except for a mild hypoproteinemia and hypoalbuminemia (Figure 2E).

Progressive pulmonary infiltrates evident in pulmonary radiographs. Radiographic scores at 1 and 3 dpi were increased as compared with baseline values (Figure 3A) and indicated the presence of progressive pulmonary infiltrates consistent with viral pneumonia likely with concurrent noncardiogenic pulmonary edema secondary to ARDS (Figure 3B). At 1 dpi, radiographic changes consistent with viral pneumonia were present in the thoracic radiographs of 5 (45%) of 11 mink. Of these 5, 4 had evidence of a mild-to-moderate ground glass/unstructured interstitial pattern and the remaining animal had a moderate-to-marked alveolar pattern affecting multiple lung lobes. Interestingly, this animal had progressive multifocal grade 3 and 4 pulmonary infiltrates at 2 dpi prior to euthanasia (Figure 3). At 3 dpi, 8 of the 9 remaining animals displayed disease progression that was characterized by increased severity and more extensive distribution of identified multifocal alveolar pattern (grade 3 to 4).

The remaining animal was monitored for resolution of disease over 28 days. Changes consistent with viral pneumonitis were first detected at 3 dpi, with the most severe changes noted at 5 dpi characterized by alveolar pattern in both caudal lung lobes. These changes began to resolve at 7 dpi with complete resolution noted at 14 dpi (Supplemental Figure 4).

Pathological changes in mink resemble severe human COVID-19 pulmonary damage and coagulopathy. Necropsy of all animals was performed immediately after euthanasia. The lung weight/BW ratio was assessed to estimate the extent of pulmonary edema, and the ratio was significantly increased in infected animals compared with uninfected controls (Figure 4A). There were varying degrees of gross pulmonary pathology evident in all 10 animals euthanized at 2 or 3 dpi, with 100% of some lungs affected (Figure 4B). Grossly, lungs were hyperemic, and several animals had undergone pulmonary hepatization (Figure 4B).

Histopathologic lesions associated with SARS-CoV-2 were restricted to the nasal turbinates and lungs of animals euthanized at 2 or 3 dpi. Nasal turbinates were characterized by a marked neutrophilic rhinitis with multifocal respiratory epithelial degeneration, necrosis, and loss. Nasal cavities were filled with an exudate composed of abundant neutrophilic and necrotic debris. There was rare neutrophilic infiltration of olfactory epithelium (Figure 5). Pulmonary pathology was more severe in 3 of 10 animals euthanized at 2 or 3 dpi. Lesions consisted of moderate to marked vascular congestion (Figure 4, C and D) with thickening of the alveolar septa by edema, fibrin, and cellular infiltrate. Multifocal fibrin thrombi were identified in the vasculature of regions of congestion (Figure 4, E and F). Alveolar lumina often contained abundant edema fluid, fibrin, and increased number of alveolar macrophages. There was a moderate lymphoplasmacytic perivascular cuffing. Bronchial and bronchiolar epithelium was generally unaffected. The remaining 7 animals had mild congestion and moderate lymphoplasmacytic perivascular cuffing with a mild increase in alveolar macrophages. Lungs were stained with phosphotungstic acid-hematoxylin (PTAH) as a marker for fibrin deposits to confirm changes in pulmonary coagulation (Figure 4, G and H). SARS-CoV-2 antigen was observed predominately in pulmonary macrophages, although it was unclear if this was the result of replication or phagocytosis of viral antigen (Supplemental Figure 5, A and B). Multifocal SARS-CoV-2 antigen positivity was identified in bronchial epithelium and type I and II pneumocytes and bronchiolar epithelium (Supplemental Figure 5, C and D).

Viral shedding is detected as early as 1 dpi in experimentally infected mink. Viral RNA was detected from all animals beginning at 1 dpi, with the highest viral RNA loads detected in oral and nasal swabs. In nasal, oral, and rectal swabs, both genomic RNA (gRNA) and subgenomic RNA (sgRNA) were detected, with sgRNA as a marker for viral replication. Viral RNA was readily detected in both oral and nasal swabs (Figure 6, A and B). Viral RNA was also detected in rectal swabs collected from 4 of 11 (36%) animals at 1 dpi and 3 of 9 (33%) animals at 3 dpi (Figure 6C). Fur swabs were collected to estimate the risk of handlers and processors in the fur industry; gRNA was detected from most animals (Figure 6D). In the sole animal that survived until 28 dpi, viral RNA was detected in nasal swabs until 7 dpi and oral swabs until 10 dpi (Supplemental Figure 3C).

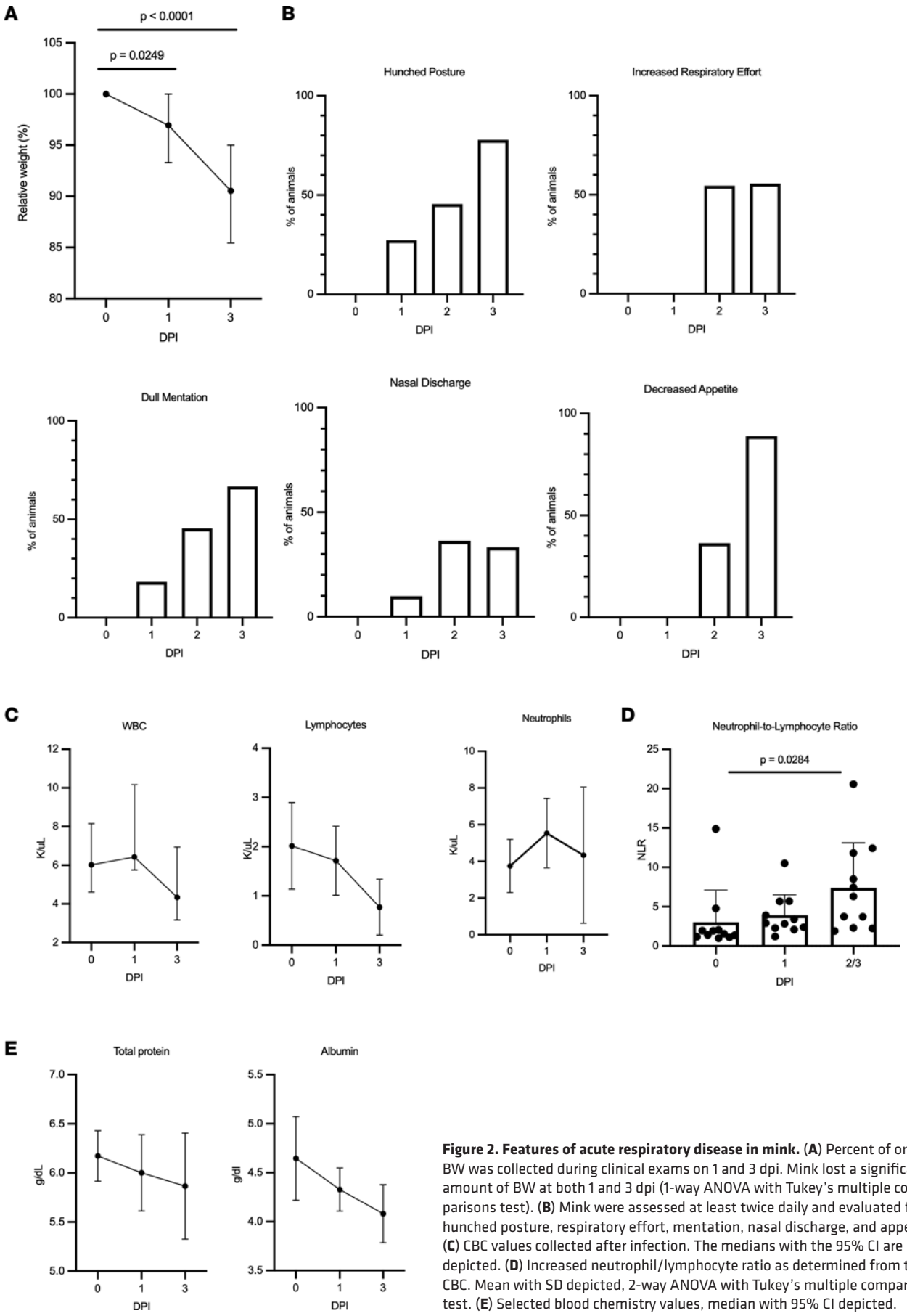

Figure 2. Features of acute respiratory disease in mink. (**A**) Percent of original BW was collected during clinical exams on 1 and 3 dpi. Mink lost a significant amount of BW at both 1 and 3 dpi (1-way ANOVA with Tukey's multiple comparisons test). (**B**) Mink were assessed at least twice daily and evaluated for hunched posture, respiratory effort, mentation, nasal discharge, and appetite. (**C**) CBC values collected after infection. The medians with the 95% CI are depicted. (**D**) Increased neutrophil/lymphocyte ratio as determined from the CBC. Mean with SD depicted, 2-way ANOVA with Tukey's multiple comparisons test. (**E**) Selected blood chemistry values, median with 95% CI depicted.

Infectious virus was detected in most oral and nasal swabs at 1 (8 of 9, 89%) and 3 (7 of 8, 88%) dpi. Low amounts of infectious virus were detected in 1 rectal swab at 1 dpi (1.5 $\log_{10}$ $TCID_{50}$/mL) and 1 fur swab at 3 dpi (0.75 $\log_{10}$ $TCID_{50}$/mL). Infectious virus was detected in the surviving animal until 7 dpi in nasal swabs and 10 dpi in oral swabs (Figure 6, A and B).

High viral load in respiratory tract of SARS-CoV-2–infected mink. At necropsy, 37 tissues were collected from each animal and analyzed for the presence of both gRNA and sgRNA. gRNA and sgRNA were detected in the tissues from all animals necropsied at 2 or 3 dpi (Figure 7 and Supplemental Figure 6). While viral RNA was detected in multiple organ systems, the highest viral loads were detected in respiratory tissues (Figure 7, A and B). Within the respiratory tract, the highest viral loads were detected in the upper (nasal turbinate) and lower (all lung lobes) as compared with the midrespiratory tract (trachea, right and left bronchus). In addition, high levels of viral RNA were detected in the frontal lobe, cerebellum, and brainstem (Supplemental Figure 6). Despite high levels of viral RNA, SARS-CoV-2 antigen was not observed in the olfactory bulb, cerebral cortex, or brainstem (Supplemental Figure 7); however, low titers of live virus (2–3 $\log_{10}$ $TCID_{50}$/g) were recovered from the CNS of 6 individuals. The respiratory tract was tested for the presence of infectious virus, with the majority of infectious virus found in the upper and lower respiratory tract (Figure 7C).

Within-host evolution of SARS-CoV-2 in mink indicates potential for rapid adaptation. SARS-CoV-2 genomes were deep sequenced for 23 oral swabs and 10 lung tissue samples and the SARS-CoV-2 inoculum diluent used in the experimental challenge (Supplemental Table 1). The deep sequencing runs yielded an average of 88,686 reads mapped for each sample (Supplemental Table 1). The 1 sample for which fewer than 50,000 reads were recovered was not used in subsequent analyses. Direct comparison of intrahost single nucleotide variants (iSNVs) detected at minor allele frequency thresholds of 3% and 5% showed a lack of concordance between technical replicates (Supplemental Figure 8), regardless of the SARS-CoV-2 genome copy number (Supplemental Figure 9A) or the number of sequencing reads mapped for the sample (Supplemental Figure 9B). These results are consistent with findings in other deep viral genome sequencing efforts (20, 21) and the need for tempered conclusions with the detection of low-level variants and small data sets. Therefore, we focus on changes in consensus sequence relative to the inoculum. Consensus sequences were largely unchanged from the SARS-CoV-2 inoculum sequence in all samples with the exception of a nonsynonymous mutation in the gene encoding nsp6 (L260F), which appeared enriched in the lung tissue samples of 5 mink relative to the inoculum and the oral swab samples (Figure 8). This mutation was identified 8 times in 1,064 available mink-associated SARS-CoV-2 genome sequences recovered from GISAID, including a farmed mink in the United States (EPI_ISL_1014945) in October 2020, 3 mink in the Netherlands (EPI_ISL_523102, 577749, and 523102) in May and August 2020, and 4 mink in Latvia (EPI_ISL_8514994, 8514995, 8514997, and 4548647; Supplemental Table 2) in July and September 2021.

Seroconversion in surviving mink by 14 dpi. We analyzed serum for the development of a neutralizing Ab response. All animals had a titer of less than 20 prior to challenge, and only the surviving animal developed a measurable neutralizing response. This animal seroconverted by 14 dpi with a peak neutralizing titer of 960, which decreased to a titer of 640 at euthanasia at 28 dpi.

Discussion

The continued emergence of SARS-CoV-2 variants of interest and variants of concern highlight the urgent need for animal models that consistently recapitulate the spectrum of disease in patients with COVID-19. Overall, the pseudotype entry data from this study demonstrate comparable spike entry between human and mink ACE2, supporting the suitability of mink for modeling SARS-CoV-2 infection and COVID-19 diseases.

Humans infected with SARS-CoV-2 present with a spectrum of clinical disease that ranges from asymptomatic infection to severe disease characterized by respiratory distress, sepsis, or multiorgan failure. Currently, animal models of SARS-CoV-2 either do not develop severe respiratory disease or are not amendable to repeated clinical measurements such as thoracic radiographs and clinical pathology due to their small size (1). Most human infections are confined to the upper respiratory tract. Mild or early disease manifests with nonspecific symptoms that can include fatigue, fever, headache, loss of smell and taste, congestion, and fever (22). Progression into severe disease is typically presented as worsening respiratory disease, hypoxemia, and radiographic lesions, with endpoint markers that can include coagulopathies, thromboembolism, acute kidney injury, and ARDS (22–25). Infected mink displayed clinical disease consistent with worsening human COVID-19. They consistently demonstrated a greater degree of weight loss than that reported in nonhuman primates or hamsters in the days following infection. Increased respiratory

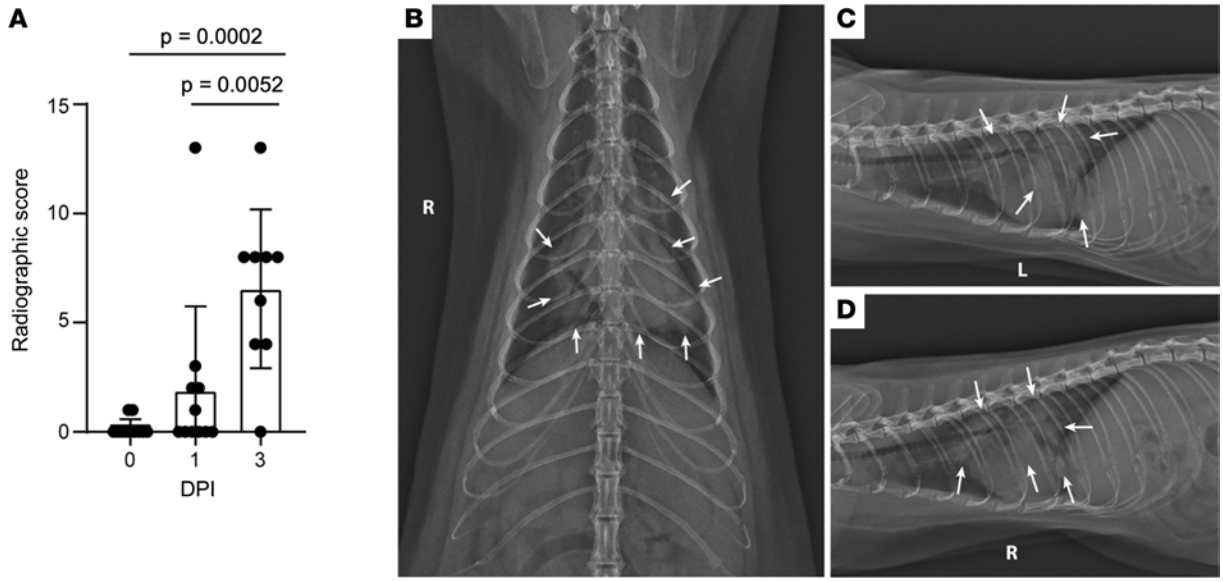

Figure 3. Severe radiological changes after infection with SARS-CoV-2. (A) Compiled radiographic scores. Bar graph depicts the mean with SD and individuals, ordinary 1-way ANOVA with Tukey's multiple comparisons test. Radiographs demonstrate multifocal pulmonary infiltrates, most severe in the left and right caudal lung lobes depicted in the (**B**) dorsoventral, (**C**) left lateral, and (**D**) right lateral radiographs on evening at 2 dpi. Arrows depict grade 4 pulmonary disease in the left and right caudal lung lobes with grade 3 pulmonary disease in the right middle lung lobe and cranial subsegment of the left cranial lung lobe.

effort and tachypnea in mink mark progression into severe COVID-19. This study did not look at odor discrimination; however, neutrophilic infiltrate in olfactory epithelium could suggest a loss of smell that resulted in decreased appetite. Interestingly, while multiple field reports of fur farm outbreaks commonly report nasal discharge, this was not a consistent finding in these mink.

Features of CBCs of patients with COVID-19 include leukopenia, lymphopenia, thrombocytopenia, and an increased NLR (14, 22, 26, 27). While we were unable to rule out a stress leukogram resulting in increased NLR, this finding has been reported in ferrets infected with H5N1 (28) and approximates critically ill human patients with COVID-19, where NLR can be used as a prognostic indicator (26). Interestingly, the NLR ratio for the single surviving animal was highest at 5 dpi, when the most severe changes were observed on thoracic radiographs. Mink displayed minimal to mild hypoproteinemia and hypoalbuminemia in the face of clinical dehydration, indicating a true hypoproteinemia. During acute disease, albumin can act as a negative-phase protein, and hypoalbuminemia has been associated with poor outcomes in patients with COVID-19 (29, 30).

One important hallmark of severe human COVID-19 is progression to ARDS. The Berlin Definition of ARDS addresses timing, thoracic imaging, the origin of thoracic edema, and the degree of hypoxemia (24). Our high-dose intratracheal inoculation likely contributed to the acute presentation of disease; however, high-dose inoculations delivered i.n. and intratracheally in nonhuman primates fail to yield severe disease (6). Additional studies are necessary to better understand the course of SARS-CoV-2 infection in mink in relationship to dose, route of inoculation, and other emerging variants. Similar to the radiologic features described in humans, mink displayed bilateral ground glass opacities (31). However, unlike humans, these radiological features were not most severe in the gravitationally dependent regions (31). One theory explaining this atypical distribution is that the method of viral inoculation may have resulted in greater distribution in the caudal lung lobes as the virus was administered intratracheally in anesthetized subjects as opposed to a more passive inhalation of viral fomites. Additionally, a component of noncardiogenic pulmonary edema, secondary to ARDS, may contribute to pulmonary infiltrates and is more commonly distributed in the caudal lung lobes. The hearts were radiographically and grossly normal, indicating the pulmonary changes were not likely due to cardiogenic pulmonary edema. Finally, this study was not able to evaluate the degree of hypoxemia, a critical step in diagnosing ARDS (24). However, the histopathological changes, evidence of pulmonary infiltrates and edema on radiographs, and acute onset of clinical disease are consistent with criteria outlined by the American Thoracic Society for animal models with ARDS (32). Additional studies using advanced tools such as blood gas analysis are required to fully evaluate this model for clinical ARDS (2, 30, 33, 34).

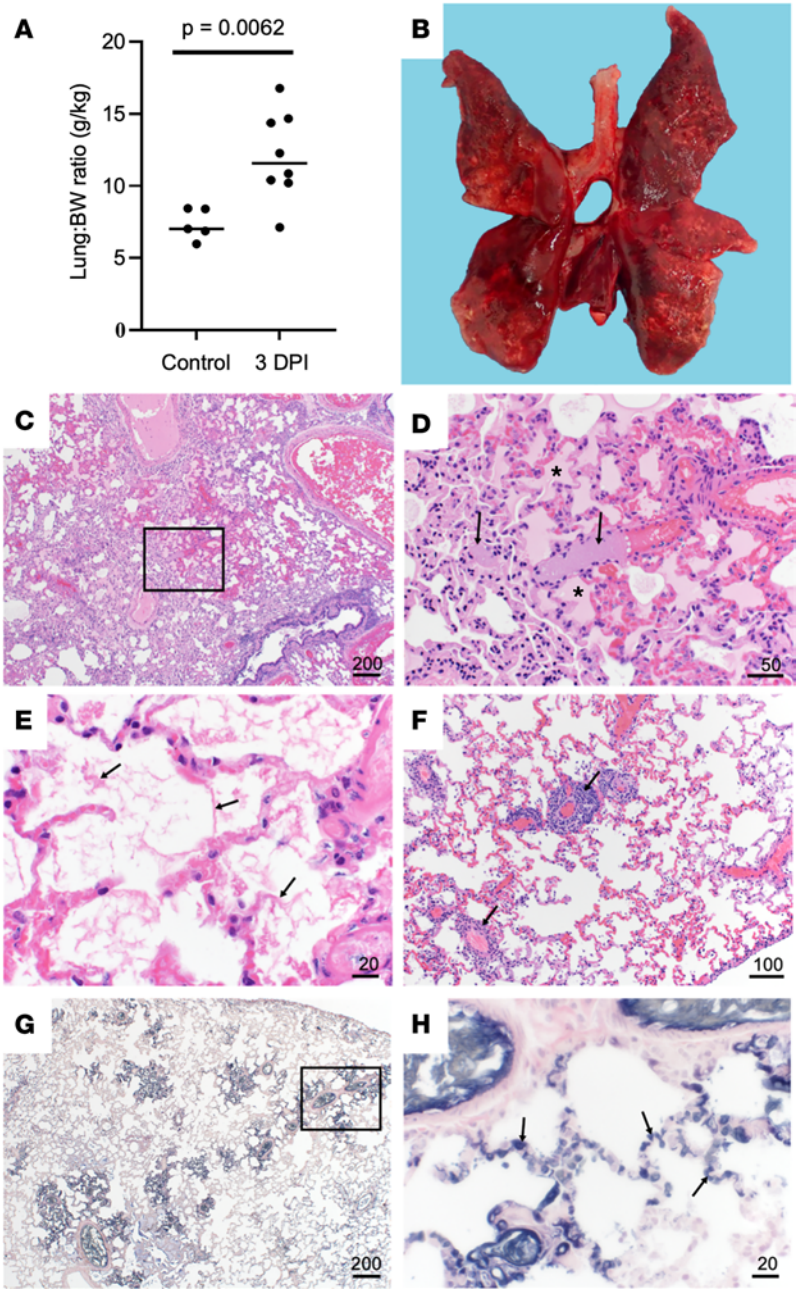

Figure 4. Pulmonary histopathology and IHC. (**A**) Lung to BW ratio, Mann-Whitney test. Graph depicts median with individuals. (**B**) Diffusely consolidated dark-mottled red lungs. (**C**) Multifocal pulmonary congestion (box). (**D**) Enlarged section of image **C**, vascular thrombi (arrows) and alveolar edema (asterisks). (**E**) Alveolar fibrin (arrows). (**F**) Lymphoplasmacytic perivascular cuffing (arrows). (**G**) Pulmonary PTAH staining (black). (**H**) Enlarged section of **G**, microthrombi (arrows). Scale bar expressed in μm in lower right corner of each image.

Histologically, diffuse alveolar disease (DAD) is an important finding in patients with severe COVID-19 disease and has not been regularly described in currently available animal models. Although not every mink had severe pulmonary pathology, all 10 animals euthanized at 2 or 3 dpi displayed pathology consistent with human COVID-19 disease (25). Animals with less severe histologic disease likely represent earlier stages in disease progression and follow-up studies are required to better understand disease progression. The multifocal fibrin thrombi, cellular infiltrate, and resulting edema in the 3 mink with histologically severe disease likely reflect a coagulopathy described in human patients with severe disease (30, 35). Additional studies focusing on D-dimer, fibrinogen, and partial thromboplastin time and activated partial thromboplastin time are required to further tease out the pathogenesis in this model (30).

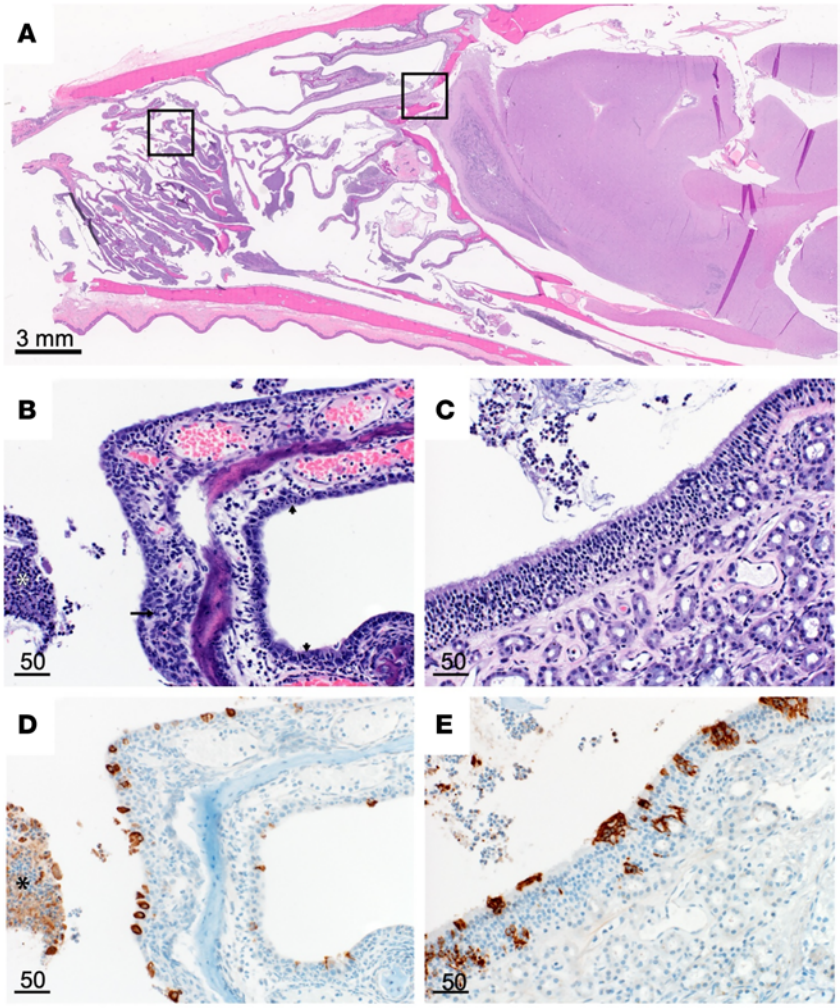

Figure 5. Nasal turbinate pathology and histopathology. (**A**) Sagittal section of skull, H&E. (**B**) Respiratory epithelium neutrophilic infiltrates (small arrows), necrotic epithelium (long arrow), and cellular exudate (asterisk). (**C**) Olfactory epithelium with cellular exudate. (**D**) Respiratory epithelium SARS-CoV-2 IHC immunoreactivity (brown) and immunoreactive cellular exudate (asterisk). (**E**) Olfactory epithelium SARS-CoV-2 IHC immunoreactivity and cellular exudate (brown). Scale bars expressed in μm unless indicated.

Outbreaks of COVID-19 on mink farms suggest the potential for novel SARS-CoV-2 variants to emerge in mink, with a high probability of spillback (8–12, 18). This study provides experimental evidence of rapid enrichment in 5 of 10 mink for L260F in the gene encoding for nsp6 in SARS-CoV-2 (Figure 8), which is hypothesized to affect viral autophagy and suppress the type I interferon response (19, 20). This mutation has been identified in multiple COVID-19 outbreaks on mink farms in the Netherlands, Latvia, and the United States. Interestingly, enrichment for the L260F mutation is most prominent in the lung tissue samples rather than the oral swabs, suggesting some tissue-specific tropism and likely a reduced probability of onward transmission. The repeated detection of the L260F mutation among COVID-19 outbreaks on mink farms through time and space supports that this mutation confers a selective advantage in mink and merits further study.

Additional preclinical models of severe COVID-19 disease are needed to better evaluate SARS-CoV-2 vaccines and therapeutics. Current models demonstrate a reduction in viral titer and a reduction of mild pathology, but no current model can fully recapitulate severe disease. In this study, we showed the utility of experimentally infected mink as a model for severe human COVID-19 disease. After infection, mink develop severe clinical disease associated with histological changes consistent with worsening human disease. Additional studies examining the impact of inoculation dose, route, and isolate will be helpful to further characterize this animal model and its utility in evaluating viral countermeasures.

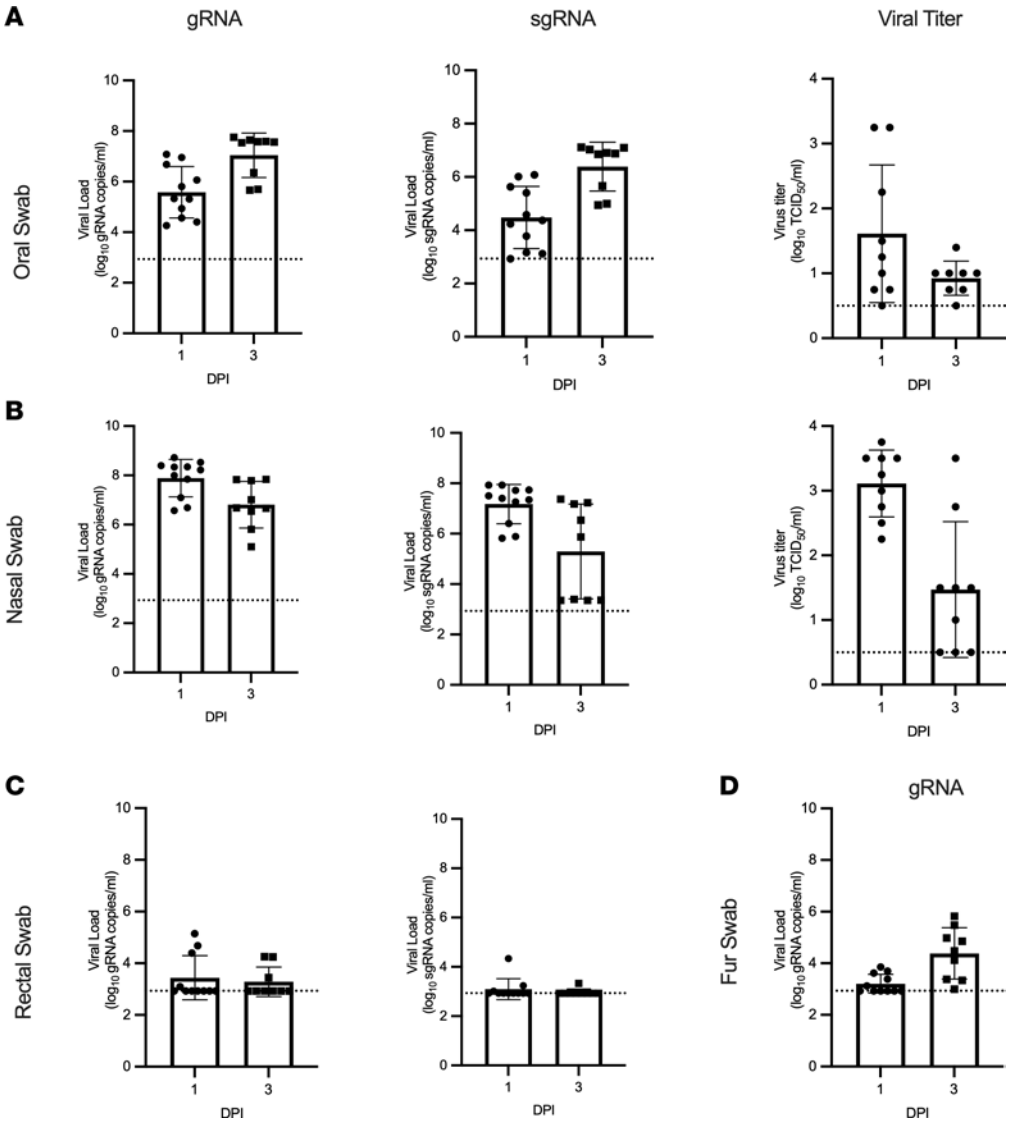

Figure 6. Viral shedding in infected mink. Oral (**A**), nasal (**B**), rectal (**C**), and fur (**D**) swabs were collected at 1 and 3 dpi and analyzed for gRNA, sgRNA, and infectious virus. Bar graphs depict the mean, SD, and individuals. Dotted line indicates the limit of detection.

Methods

Experimental design. The objective of this study is to evaluate American mink as an animal model of severe COVID-19. SARS-CoV-2 infection in American mink was determined through virological, histopathological, clinical, and radiographical analyses. Comparative analyses of functional SARS-CoV-2 entry using human and mink ACE2 were determined through a vesicular stomatitis virus pseudotyping assay. Deep viral genome sequencing was employed to study the intrahost evolutionary dynamics in the experimentally infected mink.

Mink ACE2 sequence and modeling. DNA was extracted from mink lung tissue using QIAamp DNA Tissue Kit according to the manufacturer. Mink ACE2 full-length gene was amplified using long-range PCR (LRPCR) amplification assay in 2 overlapping fragments using high-fidelity PrimeSTAR GXL DNA Polymerase (Takara Bio) as previously described (36, 37). Briefly, 50 μL LRPCR master mix contained 0.2 μM of each primer (Supplemental Table 3), 1 × PrimeSTAR GXL Buffer, 200 μM each deoxyribonucleotide triphosphate, 5 μL cDNA template, and 1.25 units of PrimeSTAR GXL DNA Polymerase (Takara Bio). The LRPCR mixture was incubated at 98°C for 2 minutes for the initial denaturation, followed by 4 cycles at 98°C for 10 seconds, 68°C for 15 seconds (–2°C per cycle), and 72°C for 10 minutes before an additional 26 cycles of 98°C for 10 seconds, 56°C for 15 seconds, and 72°C for 10 minutes. Sequencing libraries were generated using the TruSeq DNA PCR-Free library prep kit (Illumina) and sequenced on an Illumina MiSeq

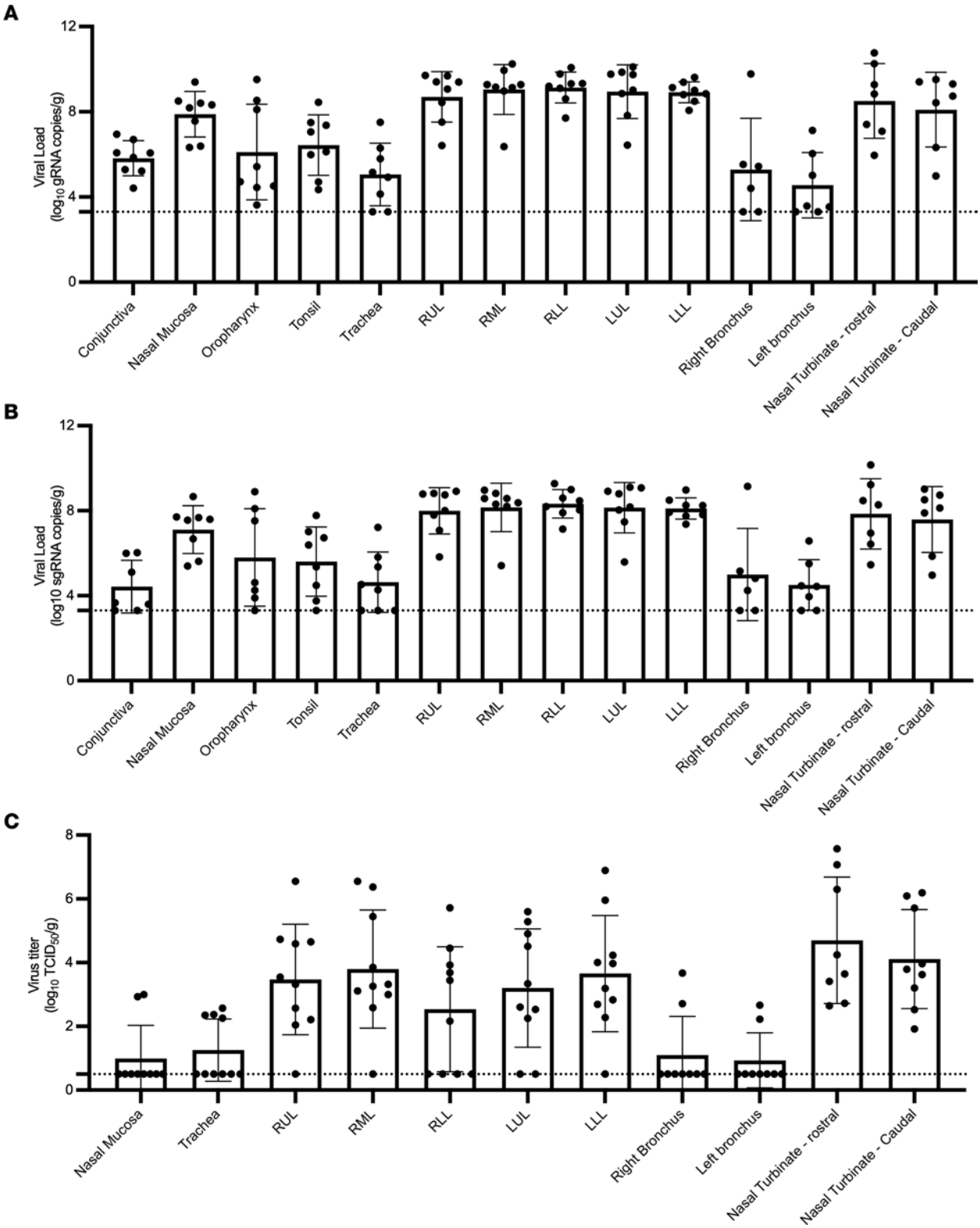

Figure 7. High levels of viral replication in the respiratory tract of infected mink. Tissues from animal euthanized at 3 dpi were analyzed for genomic (**A**), subgenomic (**B**), and infectious virus (**C**). Bar graphs depict individuals, mean, and SD. The dotted line depicts the limit of detection.

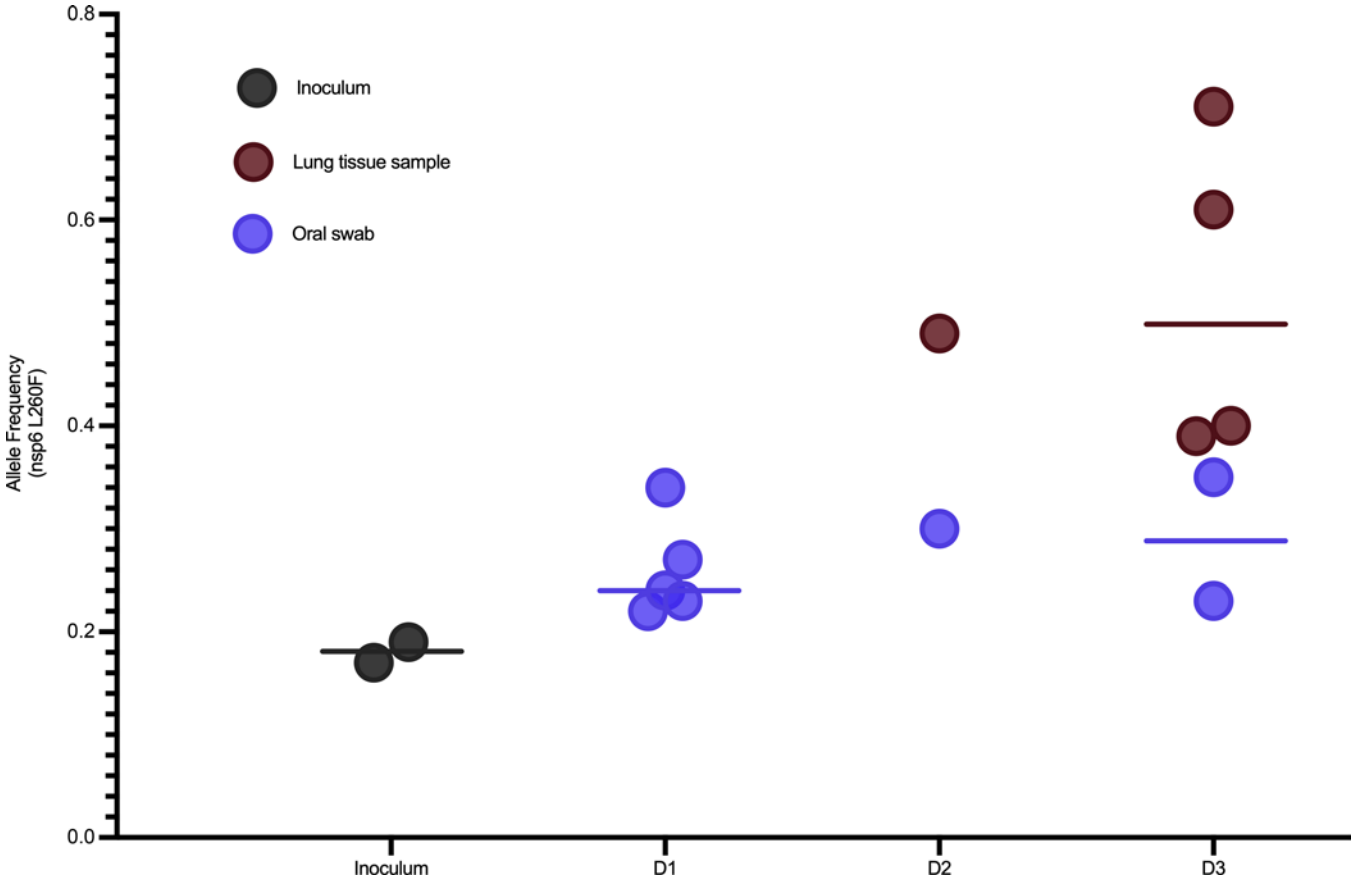

Figure 8. Enrichment of a nonsynonymous mutation (L260F) in the gene encoding nsp6 in ORF1a of SARS-CoV-2 in oral swabs and lung tissue samples of 5 experimentally challenged mink. Deep sequencing of SARS-CoV-2-positive samples show rapid enrichment for L260F in *nsp6* in lung tissue samples but not the oral swabs for 5 of 10 experimentally inoculated mink with SARS-CoV-2 genomic material detected in the lungs. Oral swab samples indicated by blue and lung tissue samples indicated by red, the line indicates group mean. Allele frequency for the L260F mutation is plotted on the *y* axis.

instrument at 2 × 151 paired-end reads. Reads were de novo assembled using SPAdes v. 3.13 (38). Sequence alignments between American mink (*Neogale vison*, sequence generated in this study) *ACE2*, European mink *ACE2* (*Mustela lutreola biedermanni*, GenBank QNC68911.1), and human *ACE2* (*Homo sapiens*, GenBank BAB40370.1) were generated using multiple alignment (39) and plotted using ESPript (40). Residues that participate in the SARS-CoV-2 RBD–ACE2 interaction, as described by Lan et al. (18), are noted below the alignment. The percentage identity between the *ACE2* sequences was calculated by Clustal Omega (41).

Structure analysis utilized the human ACE2 and SARS-CoV-2 RBD crystal structure, PDB ID 6M0J (18). Mutagenesis to show residues that differ in mink ACE2, and the Alpha and Delta variant RBD, was performed in COOT (42). The figures were generated using the PyMOL molecular graphics system (https://www.schrodinger.com/pymol).

Plasmids. The spike coding sequences for SARS-CoV-2 lineage B (hCoV-19/Denmark/DCGC-3024/2020, EPI_ISL_616802) were truncated by deleting 19 aa at the C-terminus. The S proteins with the 19 aa deletion of coronaviruses were previously reported to show increased efficiency regarding incorporation into virions of VSV (43, 44). These sequences were codon optimized for human cells, then appended with a 5′ kozak expression sequence (GCCACC) and 3′ tetra-glycine linker followed by nucleotides encoding a FLAG-tag sequence (DYKDDDDK). These spike sequences were synthesized and cloned into pcDNA3.1$^+$ (GenScript Biotech). Mink ACE2 were synthesized and subcloned into pcDNA3.1$^+$ (GenScript Biotech). All DNA constructs were verified by Sanger sequencing (ACGT).

Pseudotype production and luciferase-based cell entry assay. Pseudotype production was carried out as described previously (17). Briefly, plates precoated with poly-L-lysine (Sigma-Aldrich) were seeded with 293T cells (ATCC, catalog CRL-3216) and transfected the following day with 1,200 ng of empty plasmid and 400 ng of plasmid encoding coronavirus spike or no-spike plasmid control GFP. BHK cells were

seeded in black 96-well plates and transfected the next day with 100 ng plasmid DNA encoding human or mink ACE2 using polyethylenimine (Polysciences). After 24 hours, transfected cells were infected with VSVΔG seed particles pseudotyped with VSV-G, as previously described (17, 45). After 1 hour of incubating with intermittent shaking at 37°C, cells were washed 4 times and incubated in 2 mL DMEM supplemented with 2% FBS, penicillin/streptomycin, and L-glutamine for 48 hours. Supernatants were collected, centrifuged at 500*g* for 5 minutes, aliquoted, and stored at –80°C. BHK cells previously transfected with ACE2 plasmid of interest were inoculated with equivalent volumes of pseudotype stocks. Plates were then centrifuged at 1,200*g* at 4°C for 1 hour and incubated overnight at 37°C. Approximately 18–20 hours after infection, Bright-Glo Luciferase reagent (Promega) was added to each well at a 1:1 ratio, and luciferase was measured. Relative entry was calculated normalizing the RLU for each pseudotyped spike to the RLU average for the no-spike control.

In vitro live virus growth curves. BHK cells were seeded in 24-well plates and transfected with 500 ng of plasmid DNA encoding human ACE2, mink ACE2, or GFP. After 24 hours, cells were infected with lineage A or B.1.1.7 variants of SARS-CoV-2. After 1 hour, cells were washed 2 times with 1 mL DMEM supplemented with 2% FBS, penicillin/streptomycin, and L-glutamine. Supernatant was collected at 1, 12, 24, 48, and 96 hours following infection. RNA was extracted as described above. A viral gRNA-specific assay was used to detect SARS-CoV-2 RNA. Then, 5 μL of extracted RNA was tested with the Quantstudio 3 as described above.

Animals. A total of 17 apparently healthy adult farmed mink (*Neogale vison*) were used in this study: 11 were used for experimental infection and 6 were used as controls. All mink were prescreened and negative for SARS-CoV-2 using quantitative reverse transcription-PCR (qRT-PCR), a pancoronavirus assay (46), viral neutralization assay, and Aleutian disease using a lateral flow immunoassay (Scintilla).

The animals used in the infection study consisted of 9 females and 2 males; intake female BW range was 1.04–1.47 kg, mean = 1.18 kg, and male weights were 2.06 kg and 2.73. The females were approximately 2 years of age, the males were approximately 1 year of age. Upon arrival, whole blood from all mink was screened for Abs against SARS-CoV-2. Animals were single housed in a climate-controlled room with a fixed light/dark cycle (12-hour light/12-hour dark) for the duration of the experiment with access to food and water ad libitum with enrichment that included human interaction, commercial toys, music, and treats. All manipulations were done on anesthetized animals using Telazol (10–20 mg/kg administered s.c.).

Animal study. A total of 11 animals were inoculated intratracheally (1.7 mL) and i.n. (0.15 mL) per naris delivered using a MAD Nasal Mucosal Atomization Device (Teleflex) for a total dose of 10^5 $TCID_{50}$ delivered in 2 total mL. Animals were evaluated at least twice daily throughout the study. Clinical exams (including thoracic radiographs) were performed at 0, 1, 3, 5, 7, 10, 14, 17, 21, and 28 dpi on anesthetized animals, during which the following parameters were assessed: BW, body temperature, heart rate, respiratory rate, and radiographs. Clinical samples collected included nasal, oral, rectal, and fur swabs, and blood. Fur swabs were collected down the dorsal midline of the animal. Swabs were collected in 1 mL of DMEM supplemented with 2% FBS, 1 mM L-glutamine, 50 U/mL penicillin, and 50 g/mL streptomycin.

Radiographs. Ventrodorsal, left lateral, and right lateral thoracic radiographs were taken prior to clinical exams at 0, 1, 3, 5, 7, 10, 14, 17, 21, and 28 dpi with 0 dpi being performed prior to inoculation and serving as a baseline. Thoracic radiographs were taken immediately after animals were anesthetized and each lung lobe was evaluated by a board-certified veterinary radiologist as follows: 0 = normal lung, 1 = mild interstitial infiltrate, 2 = moderate to marked unstructured interstitial pattern, 3 = less than 25% alveolar pattern, and 4 = greater than 25% alveolar pattern.

Clinical pathology. Hematology analysis was completed on a ProCyte Dx (IDEXX Laboratories) and the following parameters were evaluated: RBCs; hemoglobin (Hb); hematocrit (HCT); mean corpuscular volume (MCV); mean corpuscular hemoglobin (MCH); mean corpuscular hemoglobin concentration (MCHC); red cell distribution width (RDW); platelets; mean platelet volume (MPV); WBCs; neutrophil count (absolute and percentage); lymphocyte count (absolute and percentage); monocyte count (absolute and percentage); eosinophil count (absolute and percentage); and basophil count (absolute and percentage). Serum chemistry analysis was completed on a VetScan VS2 Chemistry Analyzer (Abaxis) and the following parameters were evaluated: glucose; blood urea nitrogen (BUN); creatinine; calcium; albumin; total protein; alanine aminotransferase (ALT); aspartate aminotransferase (AST); alkaline phosphatase (ALP); total bilirubin; globulin; sodium; potassium; chloride; and total carbon dioxide. Clinical pathology samples were evaluated by a board-certified clinical veterinarian.

Histopathology. Histopathology and IHC were performed on mink tissues. Tissues were fixed for a minimum of 7 days in 10% neutral-buffered formalin with 2 changes. Tissues were placed in cassettes and processed with a Sakura VIP-6 Tissue Tek, on a 12-hour automated schedule, using a graded series of ethanol, xylene, and PureAffin. Embedded tissues were sectioned at 5 μm and dried overnight at 42°C prior to staining. The skulls were placed in Cancer Diagnostic acid-free EDTA for 4 weeks and the solution was changed weekly.

Tissue sections were stained with H&E. The tissues were then processed for IHC using the Discovery Ultra automated stainer (Roche Tissue Diagnostics) with a ChromoMap DAB kit (Roche Tissue Diagnostics, catalog 760-159). Specific anti-CoV immunoreactivity was detected using SARS-CoV-2 nucleocapsid Ab (GenScript Biotech) at a 1:1,000 dilution. The secondary Ab was the Vector Laboratories ImPress VR anti-rabbit IgG polymer (catalog MP-6401). To detect ACE-2, ACE-2 Ab (R&D Systems, catalog AF933) was used at a 1:100 dilution with Vector Laboratories ImPress anti-goat IgG polymer (catalog MP-7405) as a secondary Ab.

Virus and cells. SARS-CoV-2 variant B.1.1.7 (hCoV-19/England/204820464/2020, EPI_ISL_683466; designated B.1.1.7 throughout the manuscript) was obtained from Public Health Agency England via BEI Resources. The obtained passage 2 material was propagated once in VeroE6 cells (VERO C1008; ATCC, catalog CL-1586) in DMEM supplemented with 2% FBS, 1 mM L-glutamine, 50 U/mL penicillin, and 50 g/mL streptomycin. Mycoplasma testing was performed at regular intervals and no mycoplasma was detected. For sequencing from viral stocks, sequencing libraries were prepared using Stranded Total RNA Prep Ligation with Ribo-Zero Plus kit per manufacturer's protocol (Illumina) and sequenced on an Illumina MiSeq at 2 × 150 base pair reads. Low-level sequence variation was observed in the stock of B.1.1.7 (nsp6/D165G/14%, nsp6/L257F/18%, and nsp7/V11L/13%).

RNA extraction and qRT-PCR. RNA was extracted from nasal, oral, rectal, and fur swabs using the QiaAmp Viral RNA kit (Qiagen Sciences) according to the manufacturer's instructions and following high containment laboratory protocols. Tissue samples were homogenized and extracted using the RNeasy kit (Qiagen Sciences) according to the manufacturer's instructions and following high containment laboratory protocols. A viral sgRNA specific assay was used for the detection of viral RNA (48). Then, 5 μL of extracted RNA was tested with the Quantstudio 3 system (Thermo Fisher Scientific) according to instructions from the manufacturer. A standard curve was generated during each run using SARS-CoV-2 standards containing a known number of genome copies.

Viral titration. Tissue sections were weighed and homogenized in 1 mL of DMEM. Virus titrations were performed by endpoint titration of 10-fold dilutions of swab media or tissue homogenates on VeroE6 cells (VERO C1008; ATCC, catalog CL-1586) in 96-well plates. When titrating tissue homogenate, the top 3 rows of cells were washed 2 times with DMEM prior to the addition of a final 100 μL of DMEM. Cells were incubated at 37°C and 5% CO_2. The cytopathic effect was read 6 days later.

SARS-CoV-2 genome sequencing and within-host evolution. Oral swabs and lung tissue samples were collected into Trizol for RNA extraction. Then, 200 μL of 1-bromo-3-chloropropane (MilliporeSigma) was added to the Trizol/sample lysate, mixed, and centrifuged at 16,000*g* for 15 minutes at 4°C. RNA containing aqueous phase of 600 μL was collected from each sample and aqueous phase was combined with 600 μL of RLT lysis buffer (Qiagen) with 1% beta mercaptoethanol (MilliporeSigma). RNA was extracted using Qiagen AllPrep DNA/RNA 96-well system. An additional on-column DNase 1 treatment was performed during RNA extraction. All sample processing was performed using amplicon-free reagents and tools in aerosol-resistant vials. RNA quality was analyzed using Agilent 2100 Bioanalyzer (Agilent Technologies). RNA samples were quantitated by qRT-PCR targeting NSP5 using the AgPath-ID One-Step RT-PCR Buffer and Enzyme Mix (Life Technologies). The reactions were carried out in 20 μL reactions using NSP5 primers, forward (5′-CTGGCACAGACTTAGAAGGTAACTT-3′), reverse (5′-TCGATTGAGAAACCACCTGTCT-3′), and fluorescent probe (5′-6FAM-TTGACAGGCAAACAGCACAAGCAG-BHQ1-3′) (Biosearch Technologies). The qRT-PCR reactions were carried out at 50°C for 10 minutes, 95°C for 10 minutes, 55 cycles of 95°C for 15 seconds, and 60°C for 45 seconds. Data was analyzed using ABI 7900HT version 2.4 sequence detection system software (Thermo Fisher Scientific) and SARS-CoV-2 genome copy (equivalent/mL) numbers were determined by absolute quantitation method. Next-generation libraries were generated using the TruSeq DNA PCR Free Nano kit (Illumina) and the ARTIC multiplex PCR genome amplification protocol with the V3 primer scheme (www.protocols.io/view/ncov-2019-sequencing-protocol-bbmuik6w) and libraries were sequenced on an Illumina MiSeq at 2 × 250 paired-end reads. The ARTIC multiplex PCR SARS-CoV-2 genome amplification protocol has been widely used in viral genome sequencing during the COVID-19 pandemic and to study within-host dynamics of SARS-CoV-2 (22, 47).

To determine reproducibility of our assay, a subset of 12 samples determined to have high (10^4), medium (10^3), and low (10^2) SARS-CoV-2 genome copy (equivalent/mL) numbers by NSP5 qRT-PCR were selected as technical replicates. ARTIC primers and Illumina adapters were trimmed, low-quality bases and duplicate reads were filtered out, and mapping and variant calling were completed as described in the iVar and PrimalSeq pipeline described by Grubaugh et al. (48). iSNVs were included in further analysis if they passed the Fisher's exact test for variation above the mean error rate at that locus and had a depth of coverage at or above 100×. iSNVs were called with minor allele frequency (MAF) thresholds at 3% and 5% and compared with technical replicates (Supplemental Figure 8). iSNVs detected at 3% MAF were plotted against the SARS-CoV-2 genome copy number for each sample (Supplemental Figure 9A) and the number of reads mapped for each sample (Supplemental Figure 9B).

To compare variation arising in the experimentally challenged mink to variation previously detected in SARS-CoV-2 circulating at mink farms, all available mink-associated SARS-CoV-2 genomes were downloaded from GISAID from January 2020 through January 2022 (Supplemental Table 2).

Serology. Sera were heat inactivated (30 minutes, 56°C). After an initial 1:10 dilution of the sera, 2-fold serial dilutions were prepared in DMEM. Then, 100 $TCID_{50}$ of SARS-CoV02 variant B.1.1.7 was added to the diluted sera. After a 1-hour incubation at 37°C and 5% CO_2, the virus-serum mixture was added to VeroE6 cells (VERO C1008; ATCC, catalog CL-1586). The cells were incubated for 6 days at 37°C and 5% CO_2, at which time they were evaluated for cytopathic effect. The virus neutralization titer was expressed at the reciprocal value of the highest dilution of the serum that still inhibited virus replication.

Statistics. Statistical analysis was performed using GraphPad Version 8.4.3. Significance tests were performed as indicated in Methods subsections where appropriate with reported P values. $P < 0.05$ was considered statistically significant.

Study approval. All animal experiments were approved by the IACUC of Rocky Mountain Laboratories, NIH, and carried out in an Association for Assessment and Accreditation of Laboratory Animal Care International-accredited facility, according to the institution's guidelines for animal use and following the guidelines and basic principles in the *Guide for the Care and Use of Laboratory Animals* (National Academies Press, 2011), the Animal Welfare Act, United States Department of Agriculture and the United States Public Health Service Policy on Humane Care and Use of Laboratory Animals. The Institutional Biosafety Committee (IBC) approved work with infectious SARS-CoV-2 strains under BSL3 conditions. Sample inactivation was performed according to IBC-approved standard operating procedures for removal of specimens from high containment.

Author contributions

DRA and VJM conceived of the study. DRA, JL, JRS, CT, CMC, CKY, CS, JE, SNS, and VJM contributed to the methods. DRA, JL, JES, VAA, EH, MGH, CKY, CS, SWY, AMN, CKY, JRP, SNS, PWH, GS, DS, and VJM conducted the investigation. DRA, JL, CKY, VAA, PWH, GS, JRS, CS, CT, CMC, NMW, and SNS contributed to visualization. Formal analyses were conducted by DRA, JL, CKY, VAA, CM, and SNS. Funding for this research was acquired by VJM. JE and VJ contributed resources for this study. VJM and SNS supervised this study. The original draft was prepared by DRA with review and editing by DRA, SNS, JRS, and VJM. The final draft was reviewed and approved by all authors.

Acknowledgments

We would like to thank Emmie de Wit, Brandi Williamson, Neeltje van Doremalen, Sujatha Rashid, Ranjan Mukul, Kimberly Stempe, Kent Barbian, and Sarah Anzick for their assistance with the SARS-CoV-2 isolate. The following reagent was obtained through BEI Resources, National Institute of Allergy and Infectious Diseases (NIAID) of the NIH: Severe Acute Respiratory Syndrome-Related Coronavirus 2, Isolate hCoV-19/England/204820464/20200, NR-54000, contributed by Bassam Hallis. We are grateful to Hugh Hildebrandt for providing our Aleutian lateral flow test. We thank Tina Thomas, Rebecca Rosenke, and Dan Long for assistance with histology; Brian Smith, Kathy Cordova, Marissa Woods, and Taylor Saturday for technical and data assistance; Anita Mora for assistance with figures; and Rocky Mountain Veterinary Branch animal care staff for husbandry. We thank Kimmo Virtaneva and Dan Bruno for their assistance with extractions, the ARTIC protocol, and sequencing. Stacy Ricklefs assisted with the original isolate sequencing as well as the mink ACE2 sequencing. We also thank Randy Elkins, Steve Denny, and Alphie Cisar for additional support.

This work was supported by project 1ZIAAI001179-01 of the NIAID's Intramural Research Program (to VJM). The findings and conclusions in this report are those of the authors and do not necessarily represent the official position of the CDC. Use of product names is for identification purposes only and does not imply endorsement by the CDC, the NIH, or the US Government.

Address correspondence to: Stephanie N. Seifert; 240 SE Ott Road, Allen Center, Pullman, Washington 99163, USA. Phone: 509.335.3831; Email: stephanie.seifert@wsu.edu. Or to: Vincent J. Munster; 903 S 4th Street, Hamilton, Montana 59840, USA. Phone: 406.375.7489; Email: vincent.munster@nih.gov.

1. Munoz-Fontela C, et al. Animal models for COVID-19. *Nature*. 2020;586(7830):509–515.
2. Winkler ES, et al. SARS-CoV-2 infection of human ACE2-transgenic mice causes severe lung inflammation and impaired function. *Nat Immunol*. 2020;21(11):1327–1335.
3. Rosenke K, et al. Defining the Syrian hamster as a highly susceptible preclinical model for SARS-CoV-2 infection. *Emerg Microbes Infect*. 2020;9(1):2673–2684.
4. Shi J, et al. Susceptibility of ferrets, cats, dogs, and other domesticated animals to SARS-coronavirus 2. *Science*. 2020;368(6494):1016–1020.
5. Schlottau K, et al. SARS-CoV-2 in fruit bats, ferrets, pigs, and chickens: an experimental transmission study. *Lancet Microbe*. 2020;1(5):e218–e225.
6. Munster VJ, et al. Respiratory disease in rhesus macaques inoculated with SARS-CoV-2. *Nature*. 2020;585(7824):268–272.
7. Shuai L et al. Replication, pathogenicity, and transmission of SARS-CoV-2 in minks. *Natl Sci Rev*. 2021;8(3):nwaa291.
8. Richard M, et al. SARS-CoV-2 is transmitted via contact and via the air between ferrets. *Nat Commun*. 2020;11(1):3496.
9. Kutter JS, et al. SARS-CoV and SARS-CoV-2 are transmitted through the air between ferrets over more than 1 meter distance. *Nat Commun*. 2021;12(1):1653.
10. Kim YI, et al. Infection and rapid transmission of SARS-CoV-2 in ferrets. *Cell Host Microbe*. 2020;27(5):704–709.
11. Oreshkova N, et al. SARS-CoV-2 infection in farmed minks, the Netherlands, April and May 2020. *Euro Surveill*. 2020;25(23).
12. Shriner SA, et al. SARS-CoV-2 exposure in escaped mink, Utah, USA. *Emerg Infect Dis*. 2021;27(3):988–990.
13. Aguiló-Gisbert J, et al. First description of SARS-CoV-2 infection in 2 feral American Mink (*Neovison vison*) caught in the wild. *Animals (Basel)*. 2021;11(5):1422.
14. Molenaar RJ, et al. Clinical and pathological findings in SARS-CoV-2 disease outbreaks in farmed mink (*Neovison vison*). *Vet Pathol*. 2020;57(5):653–657.
15. Lassaunière R, et al. In vitro characterization of fitness and convalescent Ab neutralization of SARS-CoV-2 Cluster 5 variant emerging in mink at Danish farms. *Front Microbiol*. 2021;12:698944.
16. Enserink M. Coronavirus rips through Dutch mink farms, triggering culls. *Science*. 2020;368(6496):1169.
17. Letko M, et al. Functional assessment of cell entry and receptor usage for SARS-CoV-2 and other lineage B betacoronaviruses. *Nat Microbiol*. 2020;5(4):562–569.
18. Lan J, et al. Structure of the SARS-CoV-2 spike receptor-binding domain bound to the ACE2 receptor. *Nature*. 2020;581(7807):215–220.
19. Devaux CA, et al. Spread of Mink SARS-CoV-2 variants in humans: a model of sarbecovirus interspecies evolution. *Front Microbiol*. 2021;12:675528.
20. Lythgoe KA, et al. SARS-CoV-2 within-host diversity and transmission. *Science*. 2021;372(6539):eabg0821.
21. Tonkin-Hill G, et al. Patterns of within-host genetic diversity in SARS-CoV-2. *Elife*. 2021;10:e66857.
22. Mondello C, et al. Pathological findings in COVID-19 as a tool to define SARS-CoV-2 pathogenesis. A systematic review. *Front Pharmacol*. 2021;12:614586.
23. Berlin DA, et al. Severe Covid-19. *N Engl J Med*. 2020;383(25):2451–2460.
24. ARDS Definition Task Force, et al. Acute respiratory distress syndrome: the Berlin Definition. *JAMA*. 2012;307(207):2526–2533.
25. Konopka KE, et al. Diffuse alveolar damage (DAD) resulting from coronavirus disease 2019 infection is morphologically indistinguishable from other causes of DAD. *Histopathology*. 2020;77(4):570–578.
26. Liu J, et al. Neutrophil-to-lymphocyte ratio predicts critical illness patients with 2019 coronavirus disease in the early stage. *J Transl Med*. 2020;18(1):206.
27. Liu Y, et al. Neutrophil-to-lymphocyte ratio as an independent risk factor for mortality in hospitalized patients with COVID-19. *J Infect*. 2020;81(1):e6–e12.
28. Long JP, et al. Early indicators of disease in ferrets infected with a high dose of avian influenza H5N1. *Sci Rep*. 2012;2:972.
29. Zhang J, et al. Risk factors for disease severity, unimprovement, and mortality in COVID-19 patients in Wuhan, China. *Clin Microbiol Infect*. 2020;26(6):767–772.
30. Salinas M, et al. Laboratory parameters in patients with COVID-19 on first emergency admission is different in non-survivors: albumin and lactate dehydrogenase as risk factors. *J Clin Pathol*. 2021;74(10):673–675.
31. Swenson KE, Swenson ER. Pathophysiology of acute respiratory distress syndrome and COVID-19 lung injury. *Crit Care Clin*. 2021;37(4):749–776.
32. Matute-Bello G, et al. An official american thoracic society workshop report: features and measurements of experimental acute lung injury in animals. *Am J Respir Cell Mol Biol*. 2011;44(5):725–738.
33. Port JR, et al. High-fat high-sugar diet-induced changes in the lipid metabolism are associated with mildly increased COVID-19 severity and delayed recovery in the Syrian hamster. *Viruses*. 2021;13(12):2506.
34. Bezuidenhout MC, et al. Correlating arterial blood gas, acid-base and blood pressure abnormalities with outcomes in COVID-19 intensive care patients. *Ann Clin Biochem*. 2021;58(2):95–101.

35. McGonagle D, et al. Immune mechanisms of pulmonary intravascular coagulopathy in COVID-19 pneumonia. *Lancet Rheumatol*. 2020;2(7):e437–e445.
36. Seifert SN, et al. Long-range polymerase chain reaction method for sequencing the Ebola virus genome from ecological and clinical samples. *J Infect Dis*. 2018;218(suppl 5):S301–S304.
37. Yinda CK, et al. A novel field-deployable method for sequencing and analyses of henipavirus genomes from complex samples on the MinION Platform. *J Infect Dis*. 2019;221(suppl 4):S383–S388.
38. Bankevich A, et al. SPAdes: a new genome assembly algorithm and its applications to single-cell sequencing. *J Comput Biol*. 2012;19(5):455–477.
39. Corpet F. Multiple sequence alignment with hierarchical clustering. *Nucleic Acids Res*. 1998;16(22):10881–10890.
40. Robert X, Gouet P. Deciphering key features in protein structures with the new ENDscript server. *Nucleic Acids Res*. 2014;42(web server issue):W320–W324.
41. Madeira F, et al. The EMBL-EBI search and sequence analysis tools APIs in 2019. *Nucleic Acids Res*. 2019;47(w1):W636–W641.
42. Emsley P, et al. Features and development of Coot. *Acta Crystallogr D Biol Crystallogr*. 2010;66(pt 4):486–501.
43. Fukushi, S. et al. Vesicular stomatitis virus pseudotyped with severe acute respiratory syndrome coronavirus spike protein. *J Gen Virol*. 2005;86(pt 8):2269–2274.
44. Kawase M, et al. Protease-mediated entry via the endosome of human coronavirus 229E. *J Virol*. 2009;83(2):712–721.
45. Takada A, et al. A system for functional analysis of Ebola virus glycoprotein. *Proc Natl Acad Sci U S A*. 1997;94(26):14764–14769.
46. Holbrook MG, et al. Updated and validated Pan-Coronavirus PCR assay to detect all Coronavirus Genera. *Viruses*. 2021;13(4):599.
47. Rothe C, et al. Transmission of 2019-nCoV infection from an asymptomatic contact in Germany. *N Engl J Med*. 2020;382(10):970–971.
48. Grubaugh ND, et al. An amplicon-based sequencing framework for accurately measuring intrahost virus diversity using PrimalSeq and iVar. *Genome Biol*. 2019;20(1):8.